Proceedings of the 21st ICSMGE, Vienna, Austria, 14 – 19 June 2026. Pistrol, Adam & Schweiger (eds.)
Published by: ÖGG, Austrian Society for Geomechanics, Salzburg, Austria, ISBN 978-3-9503898-4-5
https://doi.org/10.53243/ICSMGE2026-1914

Objective modelling of failure processes in brittle materials: mesh dependence and regularisation in the material point method

González Acosta, José León
Applied Geosciences, Energy & Materials Transition, TNO, Utrecht, The Netherlands

Mánica, Miguel A.
Institute of Engineering, National Autonomous University of Mexico, Mexico City, Mexico. mmanicam@iingen.unam.mx

Vardon, Philip J.
Faculty of Civil Engineering and Geosciences, Delft University of Technology, Delft, The Netherlands

Hicks, Michael A.
Faculty of Civil Engineering and Geosciences, Delft University of Technology, Delft, The Netherlands

Gens, Antonio
Department of Civil and Environmental Engineering, Universitat Politècnica de Catalunya, Barcelona Tech - CIMNE, Barcelona, Spain

ABSTRACT: Much of our effort in numerical analysis within geotechnical engineering is devoted to evaluating the likelihood of failure in a given boundary value problem (BVP). However, certain problems occasionally require studying the post-failure behaviour of the mobilised soil mass and its resulting consequences. These large deformation analyses exceed the capabilities of conventional finite element formulations, requiring the use of specialised numerical techniques, such as the material point method (MPM), which can mitigate mesh distortion issues. However, since MPM is based on the same principles as the finite element method (FEM), it shares many of its limitations, including volumetric locking and the hourglass effect, as well as additional challenges, such as stress oscillations due to material points crossing element boundaries. Furthermore, when combined with a constitutive description exhibiting softening, MPM can lead to non-objective results with a pathological dependence on the adopted mesh and poor convergence properties. Within this context, the present work addresses the importance of regularisation in MPM for the objective simulation of localised deformations in the presence of brittle materials. A nonlocal approach was incorporated within an existing MPM framework and applied to the simulation of a number of simple BVPs with a softening material. As in conventional FEM simulations, results without regularisation showed a more brittle global response and larger strains and displacements as the element size was reduced. Furthermore, and particularly relevant for studying the consequences of a given collapse, run-out distances were shown to depend on the mesh resolution. On the other hand, regularised simulations exhibited consistent behaviour, with a global response and a configuration of localised deformations that were approximately independent of the employed mesh. However, it was demonstrated that stress oscillation issues must also be addressed when softening is considered to prevent numerical instabilities.

KEYWORDS: brittle soil, material point method, mesh dependency, nonlocal regularisation, stress oscillations.

1 INTRODUCTION

The material point method (MPM) has become a robust tool for analysing large deformation problems in geotechnical engineering. Based on the same theoretical foundations as the finite element method (FEM), MPM extends FEM by incorporating an additional step in which the computational mesh is reset to its original position, while material points (equivalent to integration points in FEM) retain their updated positions. This enables objective handling of large strains without mesh entanglement. MPM has been successfully applied to a wide range of geotechnical problems, including soil–structure interaction (González Acosta et al., 2021a; Sang et al., 2024), landslide initiation and propagation (González Acosta et al., 2021b; Nguyen et al., 2021), earthquake-induced ground motion (Zai et al., 2023), CPT penetration (Martinelli and Galavi, 2021), and unsaturated soil behaviour (Yerro et al. 2022).

Despite its advantages, MPM inherits several limitations from FEM, such as volumetric locking, hourglass modes, and mesh dependency during strain softening. In particular, simulations involving brittle materials often produce non-objective results due to strain localisation in narrow shear bands, resulting in mesh-dependent energy dissipation. These issues originate from the absence of an internal length scale in classical continuum formulations, which is essential for capturing the influence of the material's microstructure on the localisation process.

Although techniques such as gradient and nonlocal models have been introduced in FEM to address mesh sensitivity, their implementation in MPM remains limited. Some promising results have been reported for nonlocal regularisation in MPM (Burghardt et al., 2012; Huth et al., 2021); however, a comprehensive investigation is still lacking.

This contribution summarises the nonlocal strain-softening elastoplastic model that has been integrated into the MPM framework for simulating large deformations in quasi-brittle geomaterials, as presented in González Acosta et al. (2024) and González Acosta and Mánica (2024). The numerical framework is outlined, followed by an assessment of the model's performance through a number of benchmark boundary value problems, highlighting the benefits of nonlocal regularisation in producing objective softening behaviour.

2 NONLOCAL MPM FORMULATION

2.1 *MPM background*

As indicated earlier, the MPM formulation is, in principle, the same as that used in FEM. However, MPM introduces a series of additional computational steps that enable the simulation of large deformations. Figure 1 illustrates these computational

steps in MPM, where the black dots represent the nodes of the numerical mesh (dotted lines), and the brown markers indicate the material points, which represent the analysed body (in grey). Figures 1a and 1b illustrate two fundamental steps common to both MPM and FEM: nodal integration, which assigns stiffness and forces to the nodes, and nodal displacement, resulting from the global force balance and system stiffness. Subsequently, Figure 1c shows the key step in MPM, in which the set of material points remains in their current positions while the numerical mesh is reset to its original configuration.

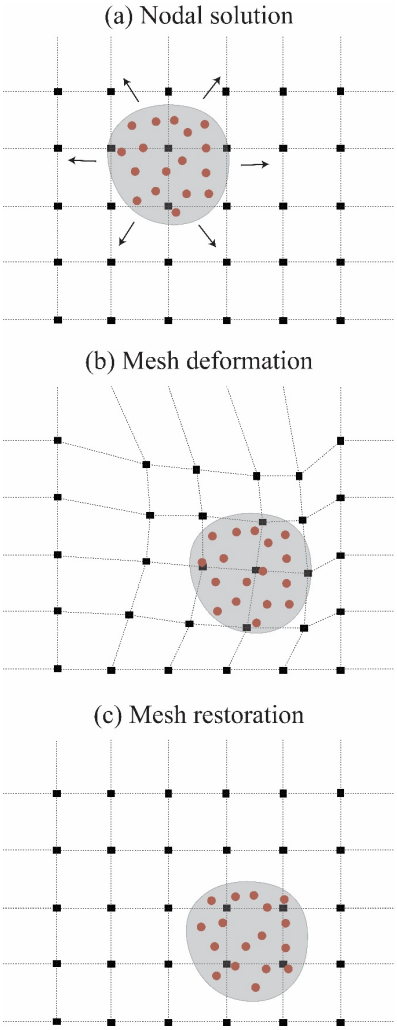

Figure 1. Fundamental steps in MPM (after González Acosta et al., 2024).

The nodal equations may be formulated in matrix notation using either an implicit or explicit scheme. For the purposes of this investigation, an implicit dynamic formulation has been adopted. The general MPM formulation is written as

$$\boldsymbol{Ma} + \boldsymbol{Ku} = \boldsymbol{f}^{\text{ext}} - \boldsymbol{f}^{\text{int}} \tag{1}$$

where $\boldsymbol{M}$ and $\boldsymbol{K}$ are the global mass and stiffness matrices, $\boldsymbol{a}$ and $\boldsymbol{u}$ are the nodal acceleration and displacement vectors, respectively, and $\boldsymbol{f}^{\text{ext}}$, $\boldsymbol{f}^{\text{int}}$ are the vectors of external and internal forces. Subsequently, applying the time integration technique proposed by Newmark (1959), Equation (1) can be expressed as:

$$\left(\boldsymbol{K} + \frac{4\boldsymbol{M}}{\Delta t^2}\right)\Delta\boldsymbol{u} = \boldsymbol{f}^{ext} - \boldsymbol{f}^{int} - \boldsymbol{m}\left(\frac{4\boldsymbol{u}}{\Delta t^2} - \frac{4\boldsymbol{v}}{\Delta t} - \boldsymbol{a}\right) \tag{2}$$

where Δt is the time discretization step, and $\boldsymbol{v}$ is the nodal velocity vector.

It is important to highlight that, due to the continuous displacement of material points within the numerical mesh, stress oscillations will arise. To overcome such oscillations, several approaches have been developed. In this investigation, the double mapping approach introduced in González Acosta et al. (2020) is adopted.

2.2 *Nonlocal model*

The constitutive model used to characterise the material behaviour corresponds to a non-local elastoplastic formulation. The yield surface is defined using a hyperbolic approximation of the Mohr–Coulomb criterion, as proposed by Gens et al. (1990):

$$f = \sqrt{\frac{J_2}{f_d(\theta)} + (c^* + p_t \tan\phi^*)^2} - (c^* + p\tan\phi^*) \tag{3}$$

where p, J_2, and θ are the common stress invariants, c^* and ϕ^* are the asymptotic cohesion and friction angle, respectively, and p_t is the tensile strength. The function $f_d(\theta)$ describes the shape of the yield surface in the deviatoric plane, characterised here according to van Eekelen (1980). The model assumes a brittle material response, with isotropic, non-linear softening. The reduction of strength parameters are defined in terms of their evolution with plastic strain. For instance, the reduction in cohesion as a function of accumulated plastic deformation is expressed as:

$$c^* = \left(c^*_{\text{peak}} - c^*_{\text{post}}\right) \mathrm{e}^{-b_{\text{post}}\,\varepsilon^{\text{p}}_{\text{eq}}} + c^*_{\text{post}}\,\mathrm{e}^{-b_{\text{res}}\,\varepsilon^{\text{p}}_{\text{eq}}} \tag{4}$$

where the subscripts *peak*, *post*, and *res* refer to peak, post-peak, and residual strength values, respectively, following the terminology of Burland (1990). The parameters b_{post} and b_{res} control the rate at which the material loses strength. The variable $\varepsilon^{\text{p}}_{\text{eq}}$ is the equivalent plastic strain, which governs the softening process, and is defined here as:

$$\varepsilon^{\text{p}}_{\text{eq}} = (\boldsymbol{\varepsilon}^{\text{p}} : \boldsymbol{\varepsilon}^{\text{p}})^{1/2} \tag{5}$$

where $\boldsymbol{\varepsilon}^{\text{p}}$ is the plastic strain tensor. To introduce the nonlocal extension of the model, it is assumed that the response of a given material point depends not only on its state, but also on the states of surrounding points, weighted by a spatial function. This modelling strategy helps mitigate pathological mesh dependence observed in simulations of brittle materials (Mánica et al., 2018). In this case, the non-local formulation is obtained by replacing the local state variable in Equation (5) with its non-local counterpart:

$$\bar{\varepsilon}^{\text{p}}_{\text{eq}}(\mathbf{x}) = \int_V w(\mathbf{x}, \boldsymbol{\xi})\varepsilon^{\text{p}}_{\text{eq}}(\boldsymbol{\xi})d\boldsymbol{\xi} \tag{6}$$

where w is a weighting function that defines the relative contributions of neighbouring points $\boldsymbol{\xi}$ based on their distance from the point of interest $\mathbf{x}$. In this work, the weighting is based on the radial distance between points, following the formulation proposed by Galavi and Schweiger (2010). This introduces the parameter l_s, which controls the size of the localisation region and therefore acts as a material length scale. Additional information on the adopted non-local modelling approach can be found in Mánica et al. (2018), and its implementation in MPM is described in González Acosta et al. (2024).

3 BENCHMARKING

3.1 *Biaxial benchmark*

The first benchmark involves the simulation of a biaxial compression test, as illustrated in Figure 2. The analysis is

conducted under static conditions, meaning that inertial effects are neglected. Due to symmetry, only one-quarter of the specimen is modelled, with a height of h = 0.05 m and width w = 0.03 m. Displacements at the left and bottom boundaries are constrained in the normal direction to represent symmetry, while a constant confining pressure P = 100 kPa is applied at the top and right boundaries. This value also defines the initial isotropic stress state at all material points.

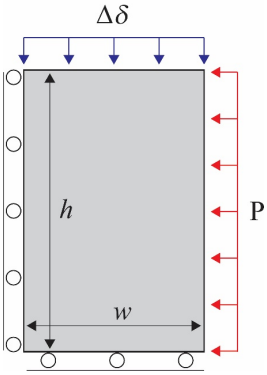

Figure 2. Geometry and boundary conditions of the simulated biaxial test.

Loading is applied via a prescribed vertical displacement at the top boundary, incremented by $\Delta\delta = 1.0 \times 10^{-5}$ m, up to a total value of δ = 0.00226 m. Horizontal displacements at the top are fixed to induce a non-homogeneous stress–strain field, favouring the onset of localisation. The material parameters used, summarised in Table 1, closely follow those employed in Mánica et al. (2018).

Table 1. Material properties of the simulated biaxial test.

Parameter	Value
Young's Modulus, E	20,000 kPa
Poisson's ratio, ν	0.2
Initial asymptotic friction angle, ϕ^*_{ini}	20°
Peak asymptotic friction angle, ϕ^*_{peak}	20°
Residual friction angle, ϕ^*_{res}	15°
Initial asymptotic cohesion, c^*_{ini}	200 kPa
Post-rupture asymptotic cohesion, c^*_{post}	0 kPa
Initial tensile strength, $p_{t\,\text{ini}}$	0 kPa
Post-rupture tensile strength, $p_{t\,\text{post}}$	0 kPa
Post-rupture softening rate, b_{post}	10
Residual softening rate, b_{res}	2
Non-associativity constant, ω	1

Simulations are performed using both the standard and regularised MPM for various mesh resolutions, with element sizes l_{ele} of 0.0033, 0.002, 0.0014, and 0.001 m. Figure 3 presents the resulting load–displacement curves. As expected, the non-regularised MPM exhibits mesh-dependent behaviour, with increased brittleness as the mesh is refined. For the regularised MPM, a length scale parameter l_s = 0.01 m is employed, fulfilling the criterion $l_s \geq l_{\text{ele}}$, thereby ensuring adequate averaging over neighbouring points.

With regularisation, the load–displacement response becomes mesh-independent, with nearly identical curves for all element sizes, except for the coarsest mesh. It is worth noting that the minimum required element size for accurate regularisation depends on the interpolation and number of integration points. In this case, with the use of four-noded linear elements, with four material points per element, the results suggest a smaller minimum size, approximately 0.2 l_s.

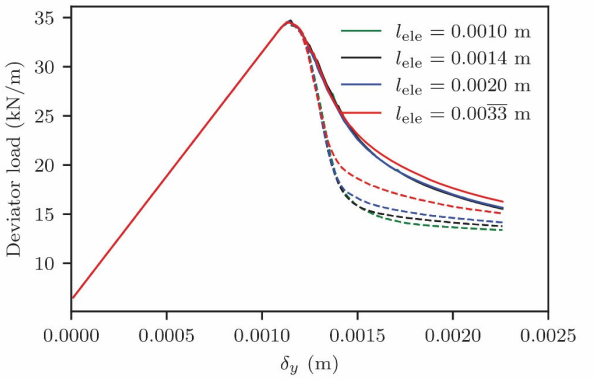

Figure 3. Load vs. displacement curves from the biaxial test simulation obtained with the non-regularised (dashed lines) and regularised (solid lines) MPM and for different element sizes l_{ele}.

Figures 4 and 5 show contours of deviatoric strains ε_q. In the non-regularised MPM (Figure 4), localisation becomes increasingly narrow and with higher strains with mesh refinement. In contrast, the regularised MPM (Figure 5) produces a consistent localisation band width (close to l_s) and similar strain magnitudes across meshes, consistent with findings in Mánica et al. (2018).

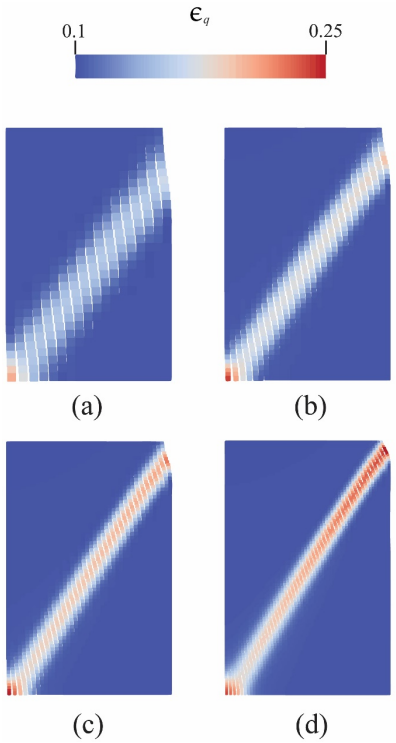

Figure 4. Contours of deviatoric strains and position of material points from the biaxial test simulation obtained with the non-regularised MPM using element sizes l_{ele} of (a) 0.0033, (b) 0.002, (c) 0.0014, and (d) 0.001 m.

3.2 *Bearing capacity benchmark*

The second benchmark is schematically illustrated in Figure 6, where a rigid shallow foundation is driven into the ground at a rate of $\Delta\delta = 2.5 \times 10^{-3}$ m per load increment. The interface between the foundation and the soil is assumed to be perfectly rough, preventing any slip and ensuring that the penetration occurs without lateral movement.

The model domain is 14 m wide and 8 m high, with displacements fixed in the normal direction at the bottom and side boundaries. A zero-stress boundary condition is applied at the ground surface. The foundation itself has a width of 1.5 m and a height of 3 m. The material properties are similar to those in Table 1, except for the changes indicated in Table 2, which were made to obtain a well-defined failure mechanism. The length scale parameter is l_s = 0.8 m for the regularised simulations.

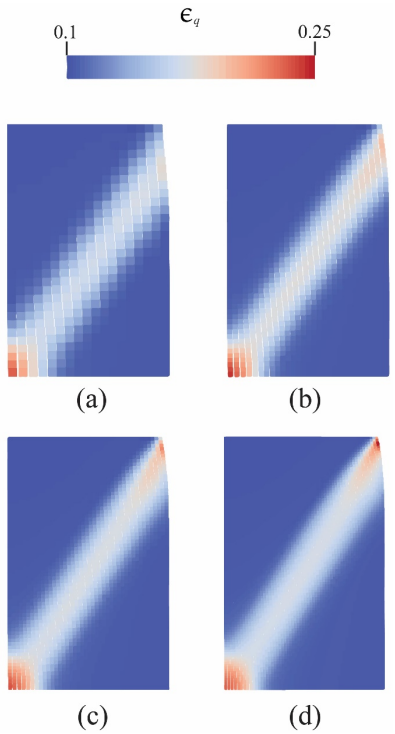

Figure 5. Contours of deviatoric strains and position of material points from the biaxial test simulation obtained with the regularised MPM using element sizes l_{ele} of (a) 0.0033, (b) 0.002, (c) 0.0014, and (d) 0.001 m and a length scale parameter l_s = 0.01 m.

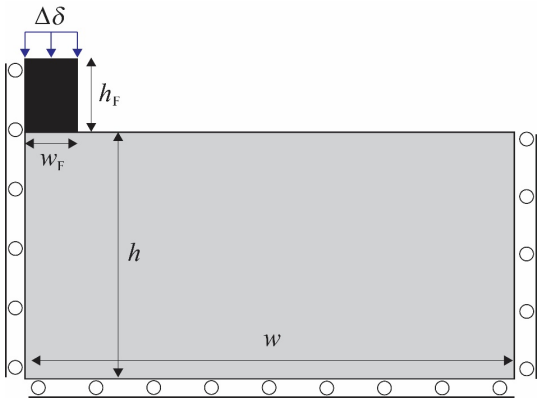

Figure 6. Geometry and boundary conditions of the shallow foundation simulation.

Figure 7 presents contours of normalised deviatoric strains and the positions of material points at a foundation penetration of 0.3 m. All simulations exhibit the typical Prandtl-type failure mechanism. However, the standard MPM results show two notable issues: (1) higher concentrations of deviatoric strain and (2) a secondary vertical shear band forming below the bottom right corner of the foundation, which becomes more pronounced with finer meshes. This secondary shear path is not present in the regularised simulations.

These differences are further illustrated in Figure 8, which shows the load–displacement responses. Although all simulations reach similar peak loads, the standard MPM exhibits increased brittleness and mesh sensitivity in the post-peak regime, with more pronounced softening as element size decreases. In contrast, regularised simulations display more consistent behaviour, largely independent of the mesh resolution. This confirms the effectiveness of the nonlocal regularisation in providing mesh-objective results in this bearing capacity problem.

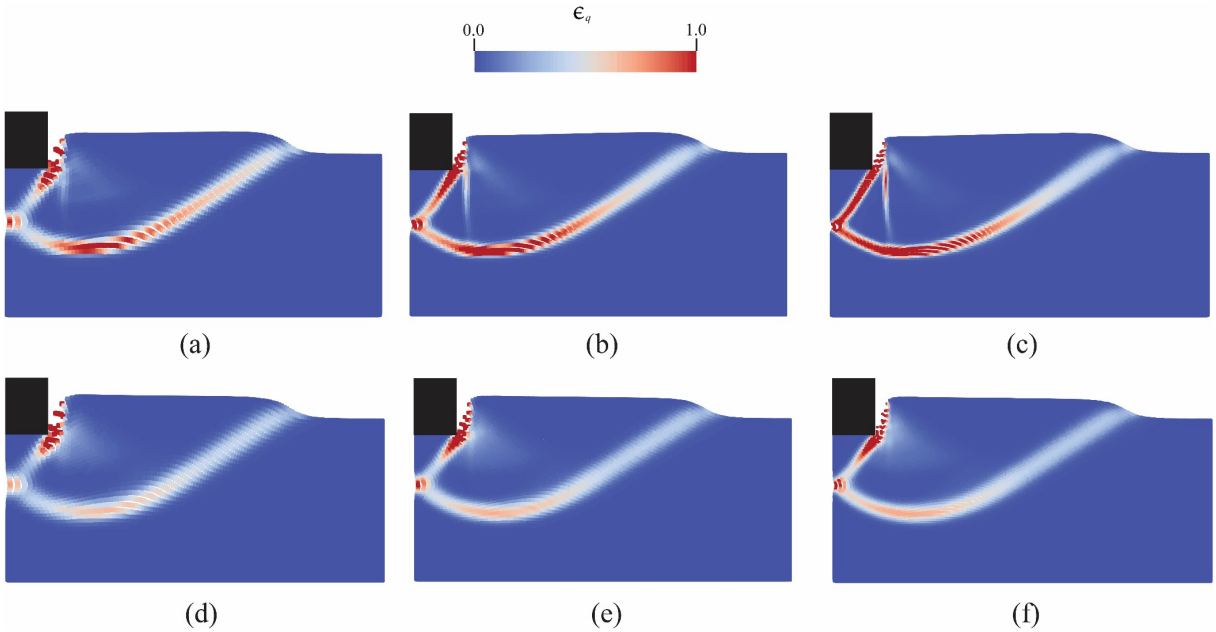

Figure 7. Contours of the normalised deviatoric strains and positions of material points from the shallow foundation simulation, obtained with (bottom row) and without (top row) regularisation, using element sizes of 0.25, 0.13, and 0.1 m (from left to right).

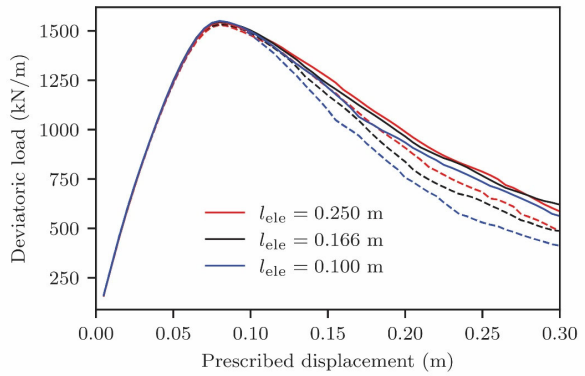

Figure 8. Load-displacement curves from the shallow foundation simulation obtained with (solid lines) and without (dashed lines) regularisation.

3.3 *Vertical cut*

This final benchmark investigates the performance of the implemented nonlocal regularisation in a dynamic large deformation context. The problem involves a vertical soil cut, where gravity is gradually increased until failure occurs. A square domain with dimensions $h = w = 3$ m is adopted, as illustrated in Figure 9. At the left boundary, displacements are fixed in the normal direction, while at the base, both vertical and horizontal displacements are constrained. The material parameters are similar to those in Table 1, with the changes indicated in Table 3.

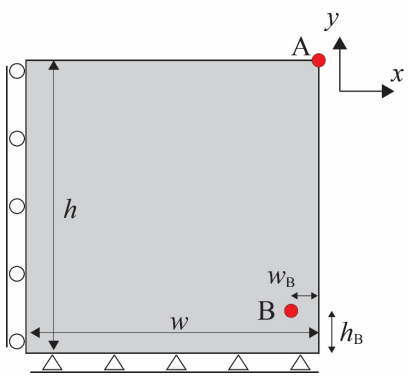

Figure 9. Geometry and boundary conditions of the vertical cut.

The initial stress state is set to zero. Gravity is increased incrementally in the vertical direction by $\Delta g = 0.1$ g every 0.001 seconds until reaching 60 g. From that point onwards, gravity is kept constant. Points A and B have been selected for monitoring purposes. While point A is located at the top right corner and used to analyse displacements, point B is situated at coordinates $h_b = 0.34$ m and $w_b = 0.22$ m and used to analyse the evolution of deviatoric stresses.

Table 2. Material properties changed for the shallow foundation simulation with respect to Table 1.

Parameter	Value
Young's Modulus, E	50,000 kPa
Poisson's ratio, ν	0.45
Initial asymptotic cohesion, c^*_{ini}	100 kPa
Post-rupture softening rate, b_{post}	5

Figure 10 shows contours of normalised deviatoric strains and the position of material points for different mesh sizes, at two time steps, for the regularised simulation using a length scale of l_s = 0.4 m. As observed, the response of the column is consistent across meshes due to the regularization approach. While some differences remain, especially for the coarsest mesh (l_{ele} = 0.1 m), they are not significant.

Figure 11 shows the evolution of deviatoric stress q at point B, defined as:

$$q = \left(\frac{1}{\sqrt{2}}\right)\sqrt{(\sigma_1 - \sigma_2)^2 + (\sigma_2 - \sigma_3)^2 + (\sigma_1 - \sigma_3)^2} \qquad (7)$$

In the standard MPM, the response is highly variable and non-monotonic, with stress increasing again once point B exits the shear band. In contrast, regularised MPM results are more stable, showing a smooth reduction of stress regardless of mesh size, thus confirming the benefit of regularisation in capturing physically consistent softening behaviour.

Finally, displacement curves in Figure 12 confirm improved mesh objectivity. It also highlights an important fact in non-regularised simulations, particularly relevant in the context of MPM: final displacements show a strong dependence on the chosen mesh.

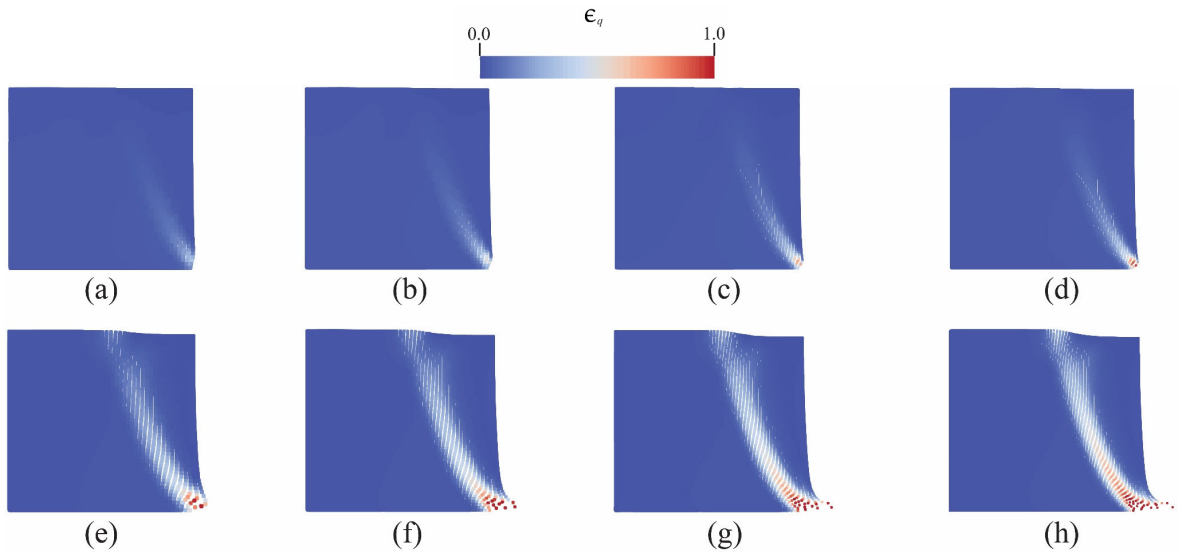

Figure 10. Contours of normalised deviatoric strains and position of material points from the vertical cut simulation obtained with the regularised MPM, for times t of 0.6 and 0.7 seconds, using element sizes of l_{ele} of (a,e) 0.1, (b,f) 0.083, (c,g) 0.071, and (d,h) 0.062 m.

Table 3. Material properties changed for the vertical cut simulation with respect to Table 1.

Parameter	Value
Young's Modulus, E	10,000 kPa
Poisson's ratio, ν	0.35
Initial asymptotic cohesion, c^*_{ini}	100 kPa
Post-rupture softening rate, b_{post}	5

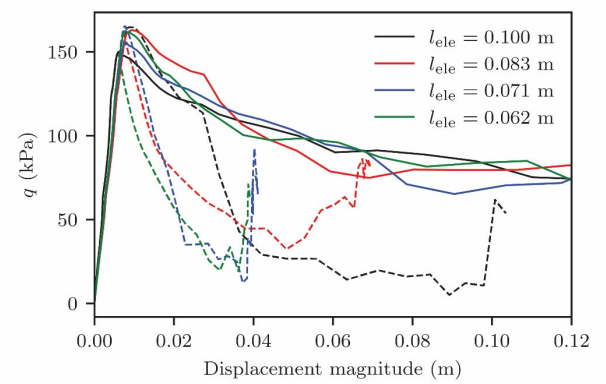

Figure 11. Evolution of deviatoric stress at point B from the vertical cut simulation obtained with the standard (dashed lines) and regularised (solid line) MPM and for different element sizes.

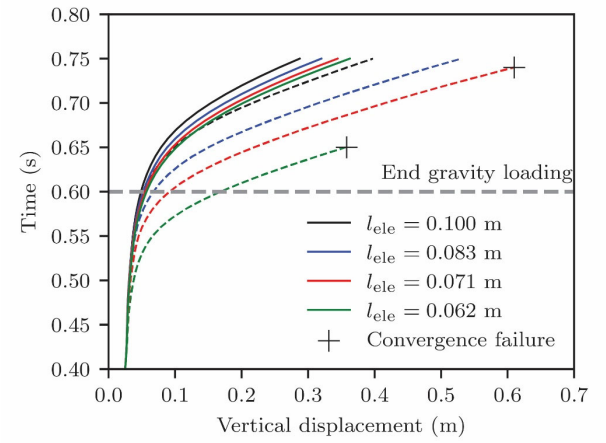

Figure 12. Displacement evolution at point A from the vertical cut simulation, comparing results from the standard (dashed lines) and regularised (solid lines) MPM for various element sizes.

4 CONCLUSIONS

This contribution presents the implementation of a nonlocal regularisation technique within the Material Point Method (MPM) framework for simulating large deformation problems in brittle geomaterials. A number of benchmark simulations were carried out to demonstrate the importance of regularisation. Due to stress oscillations, which limited the performance of the standard MPM in softening scenarios, an enhanced formulation, known as the double mapping MPM, was adopted.

The simulations showed that numerical issues commonly found in conventional finite element methods, such as mesh sensitivity and non-objective softening responses, are also present in standard MPM. As the mesh is refined, the non-regularised MPM exhibits a more brittle response, with larger strains and displacements. In dynamic analyses, the run-out distance was also affected by mesh size, which is particularly relevant when evaluating the outcome of collapse events using MPM.

In contrast, the regularised simulations provided consistent results, with both the global response and the localisation of deformation being nearly independent of the mesh. However, for the four-noded plane strain elements used in this study, the maximum element size required for effective nonlocal averaging appeared to be smaller than previously suggested, approximately 0.2 times the selected length scale parameter l_s.

5 REFERENCES

Burghardt, J., Brannon, R., and Guilkey, J. (2012). A nonlocal plasticity formulation for the material point method. *Computer Methods in Applied Mechanics and Engineering*, *225*, 55-64.

Burland, J.B. (1990). On the compressibility and shear strength of natural clays. *Géotechnique* 40 (3), 329-378.

Galavi V. and Schweiger H.F. 2010. "Nonlocal multilaminate model for strain softening analysis". *International Journal of Geomechanics*, Vol. 10, 30–44.

Gens, A., Carol, I., and Alonso, E.E. (1990). A constitutive model for rock joints formulation and numerical implementation. *Computers and Geotechnics*, *9*(1-2), 3-20.

González Acosta, J.L., and Mánica, M.A. 2024. Investigación preliminar sobre el deslizamiento de laderas utilizando el método del punto material y una regularización no local. *XXXII Reunion Nacional de Ingenieria Geotecnica (RNIG),* Ciudad de México, México.

González Acosta, J.L., Mánica, M.A., Vardon, P.J., Hicks, M.A., and Gens, A. 2024. A nonlocal material point method for the simulation of large deformation problems in brittle soils. *Computers and Geotechnics*, 172, 106424.

González Acosta, J.L., Vardon, P.J., and Hicks, M.A. 2021a. Development of an implicit contact technique for the material point method. *Computers and Geotechnics*, 130, 103859.

González Acosta, J.L., Vardon, P.J., and Hicks, M.A. 2021b. Study of landslides and soil-structure interaction problems using the implicit material point method. *Engineering Geology*, 285, 106043.

González Acosta, J.L., Vardon, P.J., Remmerswaal, G., and Hicks, M.A. 2020. An investigation of stress inaccuracies and proposed solution in the material point method. *Computational Mechanics*, 65(2), 555-581.

Huth, A., Duddu, R., and Smith, B. (2021). A generalized interpolation material point method for shallow ice shelves. 2: Anisotropic nonlocal damage mechanics and rift propagation. *Journal of Advances in Modeling Earth Systems*, *13*(8), 1 - 26.

Mánica, M.A., Gens, A., Vaunat, J., and Ruiz, D.F. 2018. Nonlocal plasticity modelling of strain localisation in stiff clays. *Computers and Geotechnics*, 103, 138-150.

Martinelli, M., and Galavi, V. 2021. Investigation of the material point method in the simulation of cone penetration tests in dry sand. *Computers and Geotechnics*, 130, 103923.

Newmark, N.M. (1959). A method of computation for structural dynamics. *Journal of the Engineering Mechanics Division*, *85*(3), 67-94.

Nguyen, T.S., Yang, K.H., Ho, C.C., and Huang, F.C. 2021. Postfailure characterization of shallow landslides using the material point method. *Geofluids*, 2021(1), 8860517.

Sang, Q., Xiong, Y., Zheng, R., Bao, X., Ye, G., and Zhang, F. 2024. A hybrid contact approach for modeling soil-structure interaction using the material point method. *Journal of Rock Mechanics and Geotechnical Engineering*, 16(5), 1864-1882.

van Eekelen H.A.M. 1980. Isotropic yield surfaces in three dimensions for use in soil mechanics. *International Journal for Numerical and Analytical Methods in Geomechanics*, Vol. 4, 89–101.

Yerro, A., Girardi, V., Martinelli, M., and Ceccato, F. 2022. Modelling unsaturated soils with the Material Point Method. A discussion of the state-of-the-art. *Geomechanics for Energy and the Environment*, 32, 100343.

Zai, D., Pang, R., Xu, B., and Liu, J. 2023. Seismic failure probability analysis of slopes via stochastic material point method. *Soil Dynamics and Earthquake Engineering*, 172, 108041.